Hybrid magnetohydrodynamic-particle simulation of linear and nonlinear evolution of Alfvén modes in tokamaks

S. Briguglio, F. Zonca, and G. Vlad
Associazione Euratom-ENEA sulla Fusione, C.R. Frascati C.P. 65, 00044—Frascati, Rome, Italy

(Received 29 September 1997; accepted 29 May 1998)

Linear and nonlinear properties of moderate-toroidal-number (n) shear-Alfvén modes in tokamaks are investigated by using a hybrid MHD-particle simulation code, which solves the coupled set of MHD (magnetohydrodynamic) equations for the electromagnetic fields and gyrocenter Vlasov equation for a population of energetic ions. The existence of unstable toroidal Alfvén eigenmodes (TAE's) and their kinetic counterpart is shown for low values of the energetic-ion pressure gradient. Above a certain threshold value, the energetic particle continuum mode (EPM) is destabilized, with growth rate fast increasing with increasing energetic-particle pressure gradient. The threshold shows an inverse dependence on n. High-n EPM's could then be unstable in realistic plasma conditions. Neglecting MHD nonlinearities, for the sake of simplicity, it is shown that nonlinear TAE saturation appears to be due to the trapping of resonant energetic ions in the potential well of the wave. Saturation of the EPM occurs instead because of a macroscopic outward displacement of the energetic-ion population, with potentially dramatic consequences on α-particle confinement; such conclusions are not modified by the inclusion of MHD nonlinearities. © *1998 American Institute of Physics.* [S1070-664X(98)01109-4]

I. INTRODUCTION

Energetic ions with typical velocity v_H of the same order of the Alfvén speed $v_A \equiv B/\sqrt{4\pi n_i m_i}$ (B is the magnitude of the equilibrium magnetic field, n_i and m_i are the bulk-ion density and mass, respectively) can be produced in tokamak plasmas both by auxiliary heating methods and by fusion reactions. Due to their high velocity, they can resonate with and possibly destabilize Alfvén modes.[1–7] Their confinement properties—of crucial importance for achieving efficient plasma heating and, therefore, ignition conditions—can in turn be strongly affected by the nonlinear interaction with the Alfvénic modes associated to such instability conditions. Therefore, significant attention has been devoted to investigations of stability properties of Alfvén modes in tokamaks.

In a periodic cylinder of length $2\pi R_0$, described by (r,θ,z) coordinates, ideal magnetohydrodynamic (MHD) shear-Alfvén oscillations have a continuous frequency spectrum $\omega^2 = k_\parallel^2(r) v_A^2(r)$, with the parallel wave vector given by $k_\parallel^2(r) = [n - m/q(r)]^2/R_0^2$. Here, n and m are the mode numbers along z and θ (''toroidal'' and ''poloidal''), respectively, and $q(r) \equiv r B_z(r)/R_0 B_\theta(r)$. The spectra corresponding to different harmonics (m,n) and (m',n') are degenerate at radial locations where $k_{\parallel m,n}^2(r) = k_{\parallel m',n'}^2(r)$. Two modes with mode numbers (m,n) and $(m+1,n)$ have, e.g., the same frequency at the radial position r_0 such that $q(r_0) = (2m+1)/2n$. These oscillations are local, since the corresponding eigenfunctions are singular at the surface where the dispersion relation is satisfied. The amplitude of any radially-extended superposition of such noncollective plasma oscillations asymptotically decays in time as t^{-1},[8] due to the phenomenon of phase mixing,[9] typical of a continuous spectrum.

In toroidal equilibria, poloidal symmetry breaking and the coupling between different poloidal harmonics remove the degeneracy of the corresponding continuous spectra and yield frequency gaps,[10] in which there can exist discrete global modes, called toroidal Alfvén eigenmodes (TAE's).[11,12] In the frame of ideal MHD such modes are marginally stable, but they can be destabilized by resonant interactions with fast particles.

When a more realistic kinetic description of the core plasma dynamics is accounted for (e.g., a small—compared to wavelength—but finite thermal ion Larmor radius), as well as other nonideal effects (e.g., those associated to resistivity), the continuous shear-Alfvén spectrum is actually resolved into a closely spaced set of discrete, strongly localized, modes: the kinetic Alfvén waves (KAW's).[1,13,14] Toroidal coupling between two counter-propagating KAW's yields a new global mode,[11] called the kinetic toroidal Alfvén eigenmode (KTAE),[15] with two different branches, characterized by frequencies close to the upper or the lower boundary of the toroidicity induced frequency gap, respectively. Moreover, coupling with KAW's tends to stabilize the TAE. This effect is very small as long as the TAE frequency is well inside the gap.[15–17] When equilibrium or nonideal effects themselves bring the TAE frequency close to the lower boundary of the gap, however, TAE can be strongly coupled to KAW's and, hence, completely stabilized. In this case KTAE's can be the most unstable gap mode.[18,19]

A more strongly growing mode has been predicted theoretically[20] when the drive due to resonant energetic particles overcomes continuum damping (or, equivalently, the damping due to the coupling to the KTAE spectrum). The new mode, called the energetic particle continuum mode (EPM), appears with completely different features from those of TAE's and KTAE's. Its frequency is mainly determined by the resonance condition with the characteristic mo-

tions of the energetic particles (in the present paper we will concentrate on the wave resonances with the transit motion of circulating particles around the torus), rather than by the frequency gap in the shear Alfvén continuum, and its radial localization is directly related to the localization of the source of instability (the energetic-particle population). Differently from the case of gap modes, it is then inadequate to look at the EPM as to existing MHD modes whose stability properties are modified by the interaction with energetic particles, or, in other words, it is not possible to investigate EPM's by treating the energetic-particle dynamics in the frame of a perturbative approach.

The growth rate of energetic-particle modes is predicted to have a much stronger dependence on β_H (defined as $\beta_H \equiv 8\pi n_H T_H / B^2$, with $T_H \equiv m_H v_H^2$, and n_H and m_H being the energetic-particle density and mass, respectively) than that of TAE and KTAE. For both gap modes and EPM's, however, the most unstable wave vectors are expected to be those satisfying the condition $k_\theta \rho \lesssim 1 \lesssim k_\perp \rho$,[7,20–23] where ρ indicates the typical excursion off the magnetic surface of the energetic particle orbit associated to the particle motion with which the mode is in resonance [i.e., the Larmor radius (ρ_L) and the drift (ρ_d) or banana (ρ_B) orbit widths].

The most relevant issue in the investigation of shear-Alfvén modes in tokamak plasmas is understanding their effects on the confinement properties of the energetic particles. Several studies[24–27] have therefore analyzed the saturation mechanisms of such modes, in order to determine the fluctuation level at which saturation takes place and the consequences on the energetic-particle transport. These analyses, however, either look at mode–mode coupling effects (while keeping the energetic particle drive fixed),[25–27] or assume weakly growing modes to justify a perturbative treatment of energetic-particle dynamics.[24] Both these approaches are then expected to be inadequate to describe the saturation of the fast-growing ''nonperturbative'' EPM.

The need for a full treatment of the nonlinear energetic-particle dynamics motivate the numerical-simulation approach presented in this paper. The hybrid MHD-gyrokinetic code[19] solves, using particle-in-cell techniques,[28] the set of $O(\epsilon^3)$-reduced MHD equations for a low-β core plasma and the Vlasov equation for energetic particles. Energetic particles contribute to the dynamic evolution of the wave fields via the energetic-particle pressure–tensor term in the MHD equations. This code, then, allows us to describe both self-consistent mode structures in toroidal equilibria and energetic-particle dynamics, as well as to get a deeper insight in how the Alfvénic modes affect the confinement of such particles.

In Ref. 19, the results on the linear stability of gap modes have been reported. Here we extend the linear analysis to the regime dominated by the EPM, and study the nonlinear saturation of both gap modes and EPM's, comparing the simulation results with the findings of existing investigations. Although the code is suited for retaining both fluid and particle nonlinearities,[29] we concentrate on the latter ones for the sake of clarity. The need for increasing computational resources associated to increasing spatial resolution sets a lower limit for the wavelength of the modes that can be simulated. In this respect, our investigation is complementary to analytical treatments, based on the high-n (with n being the toroidal mode number) assumption, presented in Refs. 20 and 30

Concerning the linear stability problem, we will show that EPM destabilization occurs for $\beta_H > \beta_{H_{th}}$, with the threshold value $\beta_{H_{th}}$ decreasing with increasing toroidal mode number n approximately as $n^{-2/3}$.

As to the nonlinear saturation, a completely novel result is found. Differently from the case of gap modes (TAE or KTAE), whose saturation can evidently be traced back to the trapping of resonant energetic particles in the potential well of the wave,[24] EPM's saturate because of a macroscopic outward displacement of the energetic-particle population. This convective motion becomes, in the EPM regime, the most important phenomenon in determining the confinement properties of energetic particles, obscuring the radial diffusion due to e.m. field fluctuations.

On the basis of these results, there is an evident need of investigations of the stability and the nonlinear dynamics of high-n EPM's. Consistently with the observed inverse dependence of $\beta_{H_{th}}$ on n, such modes could be unstable in plasmas close to ignition conditions, with negative effects on α-particle confinement.

The paper is organized as follows. In Sec. II the reduced-MHD equations are presented and their coupling with the Vlasov description of the energetic particles in gyrocenter coordinates is discussed. In Sec. III we describe the numerical method adopted to solve the model equations, with regard to both the fluctuating field determination and the particle pushing. Respective merits of the so-called δF method and the standard full-F method are compared. The distinction between ''self-consistent'' and ''perturbative'' simulations is also introduced, with the latter ones suited for a more straightforward comparison with other published analytical and numerical studies of the same problem. Those readers who are familiar with the model equations and not interested in the details of the numerical method can directly skip to Sec. IV, where the results of linear simulations are reported and the inadequacy of the perturbative treatment of energetic-particle dynamics is emphasized. Mode saturation and the effects on energetic-particle confinement are investigated in Sec. V. Conclusions and a summary of the main results are contained in Sec. VI.

II. MODEL EQUATIONS

The resistive MHD equations, with a driving term related to an energetic-particle population included, can be written in the following form:

$$\frac{d\varrho}{dt} = -\varrho \nabla \cdot \mathbf{v},$$

$$\varrho \frac{d\mathbf{v}}{dt} = -\nabla P - \nabla \cdot \mathbf{\Pi}_H + \frac{1}{c}\mathbf{J} \times \mathbf{B},$$

$$\frac{\partial \mathbf{B}}{\partial t} = -c \nabla \times \mathbf{E},$$

$$\frac{dP}{dt} = -\gamma P \nabla\cdot\mathbf{v},$$

$$\mathbf{E} = \eta\mathbf{J} - \frac{1}{c}\mathbf{v}\times\mathbf{B}, \tag{1}$$

$$\mathbf{J} = \frac{c}{4\pi}\nabla\times\mathbf{B},$$

$$\nabla\cdot\mathbf{B} = 0.$$

In the above equations, $\mathbf{v}$ is the fluid velocity, $\mathbf{J}$ the plasma current, $\mathbf{B}$ the magnetic field, $\mathbf{E}$ the electric field, ϱ and P are, respectively, the mass density and the scalar pressure of the bulk plasma, $\mathbf{\Pi}_H$ is the pressure-tensor of the hot particles, γ the ratio of the specific heats, η the resistivity, c the speed of light and $d/dt \equiv \partial/\partial t + \mathbf{v}\cdot\nabla$. This coupling scheme in terms of the energetic-particle pressure tensor is suited for a gyrokinetic treatment of such particles (see below), as observed in Ref. 31, where it was first devised and used.

The MHD equations can be simplified by expanding them in powers of the inverse aspect ratio $\epsilon \equiv a/R_0$, where a and R_0 are the minor and the major radius of the torus, respectively. This procedure has been widely used, since the first paper of Strauss,[32] both for analytical and for numerical work. At the leading order in ϵ, $O(\epsilon^2)$, and considering $\beta \approx O(\epsilon^2)$, the reduced-MHD equations describe the plasma in the cylindrical approximation. The toroidal corrections enter the equations at the next order in the inverse aspect ratio. These $O(\epsilon^3)$ equations have been first derived in Ref. 33 and their modification to include energetic particle dynamics in the form of Eqs. (1) has been proposed in Ref. 29. In terms of the poloidal-magnetic-field stream function ψ and the scalar potential ϕ, they can be written, in the cylindrical-coordinate system (R,Z,φ), in the following form:

$$\begin{aligned}
&\frac{\partial\psi}{\partial t} = -\frac{cR^2}{R_0B_0}\boldsymbol{\nabla}\psi\times\boldsymbol{\nabla}\varphi\cdot\nabla\phi - \frac{c}{R_0}\frac{\partial\phi}{\partial\varphi} + \eta\frac{c^2}{4\pi}\Delta^*\psi \\
&\qquad + O(\epsilon^4 v_A B_\varphi), \\
&\hat{\varrho}\left(\frac{D}{Dt} - \frac{2c}{R_0B_0}\frac{\partial\phi}{\partial Z}\right)\nabla_\perp^2\phi + \boldsymbol{\nabla}\hat{\varrho}\cdot\left(\frac{D}{Dt} - \frac{c}{R_0B_0}\frac{\partial\phi}{\partial Z}\right)\boldsymbol{\nabla}\phi \\
&\qquad = -\frac{B_0}{4\pi c}\mathbf{B}\cdot\nabla\Delta^*\psi - \frac{B_0}{cR_0}\nabla\cdot[R^2(\boldsymbol{\nabla}P + \nabla\cdot\mathbf{\Pi}_H)\times\nabla\varphi] \\
&\qquad\quad + O\left(\epsilon^4\varrho\frac{v_A^2}{a^2}\right),
\end{aligned} \tag{2}$$

where

$$\hat{\varrho} = \frac{R^2}{R_0^2}\varrho, \qquad \frac{D}{Dt} = \frac{\partial}{\partial t} + \mathbf{v}_\perp\cdot\nabla,$$

$$\mathbf{v}_\perp \approx -\frac{cR^2}{R_0B_0}\boldsymbol{\nabla}\phi\times\nabla\varphi,$$

$$\nabla_\perp^2 \equiv \frac{1}{R}\frac{\partial}{\partial R}R\frac{\partial}{\partial R} + \frac{\partial^2}{\partial Z^2},$$

the Grad–Shafranov operator Δ^* is defined by

$$\Delta^* \equiv R\frac{\partial}{\partial R}\frac{1}{R}\frac{\partial}{\partial R} + \frac{\partial^2}{\partial Z^2},$$

B_0 is the vacuum magnetic field at $R = R_0$ and the subscript $\perp$ denotes components perpendicular to φ. In the following, we will consider the pressure of the bulk plasma to be zero and the normalized mass density $\hat{\varrho}$ to be constant in time, with spatial dependence proportional to $q(r)^{-2}$, such as to yield the same gap frequency for different pairs of poloidal harmonics. Thus, Eqs (2) are the only equations to be solved. As boundary conditions we take a rigid conducting wall at the plasma edge.

In order to close the set of reduced MHD Equations (2), the energetic-particle pressure-tensor components can be obtained by directly calculating the appropriate velocity momentum of the distribution function for the particle population moving in the perturbed electromagnetic fields.

As a convenient choice for numerical particle pushing, and in order to avoid too severe limitations on the time-step size, it is worth[34,35] following particle evolution in the gyrocenter-coordinate system $\overline{Z} \equiv (\overline{\mathbf{R}}, \overline{M}, \overline{U}, \overline{\theta})$, where $\overline{\mathbf{R}}$ is the gyrocenter position, $\overline{M}$ is the exactly conserved magnetic momentum, $\overline{U}$ corresponds to the canonical parallel momentum and $\overline{\theta}$ is the gyrophase. This corresponds to averaging the single-particle equations of motion over the fast Larmor precession and allows one to retain the relevant finite Larmor radius effects without resolving the details of the gyromotion.

The equations of motion in the gyrocenter coordinates have been derived[19] by a straightforward extension of previous treatments.[36–38] They take the form

$$\begin{aligned}
&\frac{d\overline{\mathbf{R}}}{dt} = \overline{U}\hat{\mathbf{b}} + \frac{e_H}{m_H\Omega_H}\hat{\mathbf{b}}\times\nabla\phi - \frac{\overline{U}}{m_H\Omega_H}\hat{\mathbf{b}}\times\nabla a_\parallel \\
&\qquad + \left[\frac{\overline{M}}{m_H} + \frac{\overline{U}}{\Omega_H}\left(\overline{U} + \frac{a_\parallel}{m_H}\right)\right]\hat{\mathbf{b}}\times\nabla\ln B, \\
&\frac{d\overline{M}}{dt} = 0, \\
&\frac{d\overline{U}}{dt} = \frac{1}{m_H}\hat{\mathbf{b}}\cdot\left\{\left[\frac{e_H}{\Omega_H}\left(\overline{U} + \frac{a_\parallel}{m_H}\right)\boldsymbol{\nabla}\phi + \frac{\overline{M}}{m_H}\boldsymbol{\nabla}a_\parallel\right]\times\nabla\ln B\right. \\
&\qquad \left. + \frac{e_H}{m_H\Omega_H}\boldsymbol{\nabla}a_\parallel\times\nabla\phi\right\} - \frac{\Omega_H\overline{M}}{m_H}\hat{\mathbf{b}}\cdot\nabla\ln B.
\end{aligned} \tag{3}$$

Here, e_H, m_H and $\Omega_H \equiv e_H B/m_H c$ are, respectively, the energetic-particle charge, mass and Larmor frequency; $\hat{\mathbf{b}} \equiv \mathbf{B}/B$ is the unit vector of the equilibrium magnetic field. The fluctuating potential $a_\parallel$ is related to the stream function ψ through the relationship

$$a_\parallel = \frac{e_H}{c}\frac{R_0}{R}\psi. \tag{4}$$

The parallel electric field term in the equation for $\overline{U}$ has been suppressed, neglecting in this frame the small resistive cor-

rections to the ideal-MHD condition. Note, finally, that Eq. (3) do not contain any dependence on the gyrophase $\overline{\theta}$.

The hot-particle pressure tensor can be written, in terms of the gyrocenter coordinates, as

$$\mathbf{\Pi}_H(t,\mathbf{x}) = \frac{1}{m_H^2}\int d\overline{Z} D_{z_c\to\overline{Z}} \overline{F}_H(t,\overline{\mathbf{R}},\overline{M},\overline{U}) \left[\frac{\Omega_H \overline{M}}{m_H}\mathbf{I} + \hat{\mathbf{b}}\hat{\mathbf{b}}\left(\overline{U}^2 - \frac{\Omega_H \overline{M}}{m_H}\right)\right] \delta(\mathbf{x}-\overline{\mathbf{R}}), \tag{5}$$

where $\mathbf{I}$ is the identity tensor, $I_{ij}\equiv\delta_{ij}$, $\overline{F}_H(t,\overline{\mathbf{R}},\overline{M},\overline{U})$ is the hot-particle distribution function, $D_{z_c\to\overline{Z}}$ is the Jacobian of the transformation from canonical to gyrocenter coordinates and any superscript related to the dimensionality of the phase space has been omitted for simplicity.

The distribution function $\overline{F}_H$ satisfies the Vlasov equation

$$\frac{d\overline{F}_H}{dt} = 0, \tag{6}$$

with

$$\frac{d}{dt} \equiv \frac{\partial}{\partial t} + \frac{d\overline{\mathbf{R}}}{dt}\cdot\nabla + \frac{d\overline{U}}{dt}\frac{\partial}{\partial \overline{U}},$$

and $d\overline{\mathbf{R}}/dt$ and $d\overline{U}/dt$ given by Eqs. (3).

It has been shown[19,39–43] that, as far as regimes are considered where the distribution function can be expected to slightly depart from the equilibrium one, it is worth limiting the numerical investigation to the evolution of the perturbed part $\delta\overline{F}_H$, defined by the relationship

$$\overline{F}_H(t,\overline{\mathbf{R}},\overline{M},\overline{U}) = \overline{F}_{H0}(t,\overline{\mathbf{R}},\overline{M},\overline{U}) + \delta\overline{F}_H(t,\overline{\mathbf{R}},\overline{M},\overline{U}), \tag{7}$$

where $\overline{F}_{H0}$ is the lowest-order (''equilibrium'') distribution function.

Equation (6) can be written, in terms of $\delta\overline{F}_H$, in the form

$$\frac{d\,\delta\overline{F}_H}{dt} = S, \tag{8}$$

with

$$S \equiv -\frac{d\overline{F}_{H0}}{dt}.$$

Particle-simulation techniques consist in representing any phase-space function $G(t,\overline{Z})$ by its discretized form,

$$G(t,\overline{Z}) \equiv \int d\overline{Z}'\, G(t,\overline{Z'})\,\delta(\overline{Z}-\overline{Z}') \approx \sum_l \Delta_l G(t,\overline{Z}_l)\,\delta(\overline{Z}-\overline{Z}_l), \tag{9}$$

where Δ_l is the volume element around the phase-space marker $\overline{Z}_l$, and assuming that each marker evolves in time according to the gyrocenter equations of motion, Eq. (3). Such markers can then be interpreted as the phase-space coordinates of a set of N_{part} ''particles,'' and $G(t,\overline{Z})$ can be approximated by

$$G(t,\overline{Z}) \approx \sum_{l=1}^{N_{part}} \Delta_l(t) G(t,\overline{Z}_l(t))\,\delta(\overline{Z}-\overline{Z}_l(t)). \tag{10}$$

The time-variation of the volume element $\Delta_l(t)$ is then given by

$$\frac{d\Delta_l}{dt} = \Delta_l(t)\left(\frac{\partial}{\partial \overline{Z}^i}\frac{d\overline{Z}^i}{dt}\right)_{t,\overline{Z}_l(t)}. \tag{11}$$

For the purpose of calculating the pressure tensor components, Eq. (5), it is worth it to directly represent the quantity $D_{z_c\to\overline{Z}}\overline{F}_H$ (or $D_{z_c\to\overline{Z}}\delta\overline{F}_H$), rather than just $\overline{F}_H$ (or $\delta\overline{F}_H$), according to its discretized form,

$$D_{z_c\to\overline{Z}}(t,\overline{Z})\left\{ \begin{array}{c} \overline{F}_H(t,\overline{Z}) \\ \delta\overline{F}_H(t,\overline{Z}) \end{array}\right\} \approx \sum_{l=1}^{N_{part}} \overline{w}_l(t)\,\delta(\overline{Z}-\overline{Z}_l(t)), \tag{12}$$

with the weight factor $\overline{w}_l$ defined by

$$\overline{w}_l(t) \equiv \overline{\Delta}_l \left\{ \begin{array}{c} \overline{F}_H(t,\overline{Z}_l(t)) \\ \delta\overline{F}_H(t,\overline{Z}_l(t)) \end{array}\right\}, \tag{13}$$

and

$$\overline{\Delta}_l \equiv \Delta_l(t) D_{z_c\to\overline{Z}}(t,\overline{Z}_l(t)). \tag{14}$$

Here the upper (lower) quantity in the curly brackets refers to the full-F (δF) algorithm. From Eqs. (6), (8), and (11), and from the Liouville theorem,

$$\frac{\partial}{\partial t} D_{z_c\to\overline{Z}} + \frac{\partial}{\partial \overline{Z}^i}\left(D_{z_c\to\overline{Z}}\frac{d\overline{Z}^i}{dt}\right) = 0\ , \tag{15}$$

it is immediate to show that

$$\frac{d\overline{\Delta}_l}{dt} = 0 \tag{16}$$

and

$$\frac{d\overline{w}_l}{dt} = \left\{ \begin{array}{c} 0 \\ \overline{\Delta}_l S(t,\overline{Z}_l(t)) \end{array}\right\}. \tag{17}$$

From Eqs. (16) and (17), the convenience of the approach based on Eq. (12) is evident: numerical effort is needed neither for the time evolution of the volume-element factor $\overline{\Delta}_l$, nor for the weight factor $\overline{w}_l$ (in the full-F case). In this respect the full-F approach seems to be more convenient than the δF one. In fact, the latter is recommended as far as $\delta F \ll F$, the former when $\delta F \approx F$. It can then be worth switching from δF to full-F algorithm when the transition from a small-amplitude linear-evolution phase to a large-amplitude saturated phase occurs.

In the present paper we take $\overline{F}_{H0}$ to be Maxwellian,

$$\overline{F}_{H0} \propto n_H(\overline{\mathbf{R}}) \exp\left(- \frac{\Omega_H \overline{M} + \frac{1}{2} m_H \overline{U}^2}{T_H} \right), \tag{18}$$

where $n_H(\overline{\mathbf{R}})$ and T_H are, respectively, the energetic-particle equilibrium density and (uniform) temperature. The right hand side (RHS) of Eq. (8) is then given by

$$S(t,\overline{\mathbf{R}},\overline{M},\overline{U}) = -\overline{F}_{H0} \left\{ \frac{d\overline{\mathbf{R}}}{dt} \cdot \nabla \ln n_H + \frac{e_H}{T_H} \left[\frac{\overline{M}}{m_H} + \frac{\overline{U}}{\Omega_H} \left(\overline{U} + \frac{a_\parallel}{m_H} \right) \right] \hat{\mathbf{b}} \times \nabla \ln B \cdot \nabla \phi + \frac{e_H \overline{U}}{T_H \Omega_H m_H} \hat{\mathbf{b}} \cdot \nabla \phi \times \nabla a_\parallel \right\}. \tag{19}$$

The energetic-particle equilibrium density is taken to be

$$n_H(r) = n_{H0} \exp\left[- \left(\frac{r^2}{L_n^2} \right)^{\alpha_n} \right], \tag{20}$$

where n_{H0} is the on-axis density. The equilibrium density scale length l_n is then given by $l_n = (L_n^2/r^2)^{\alpha_n} r/2\alpha_n$.

III. NUMERICAL METHOD

A. Self-consistent treatment

The coupled sets of reduced MHD equations for the fluctuating fields—Eq. (2)—gyrokinetic equations of motion—Eqs. (3)—and evolution equations for phase-space-volume and weight factors—Eqs. (16) and (17)—for the energetic particles are integrated by the hybrid MHD-particle initial-value code.[19]

At each time step, a field solver computes the fluctuating electromagnetic potentials at the grid points of a three-dimensional (3-D) toroidal domain. Phase-space coordinates and weight factors are then evolved in the fluctuating fields, and the pressure tensor components at the grid points are updated, in order to close the MHD equations for the next time step.

The energetic-particle phase-space distribution is initially loaded according to the following recipe: (a) the kinetic energy $\overline{E} \equiv m_H \overline{U}^2/2 + \Omega_H \overline{M}$ and the pitch angle $\alpha \equiv \arccos(\overline{U}/\sqrt{2\overline{E}/m_H})$, with $0 \leqslant \alpha \leqslant \pi/2$ are determined by inversion of the cumulative distribution function;[28] (b) the parallel velocity $\overline{U}$ and the magnetic momentum $\overline{M}$ are then calculated according to the relationships $\overline{U} = \pm \sqrt{2\overline{E}/m_H} \cos\alpha$, and $\overline{M} = \overline{E}/\Omega_H \sin^2\alpha$ (note that a pair of particles, with opposite values of parallel velocity, is initialized for each choice of $\overline{E}$ and α); (c) particle positions in the meridian plane are mixed in r and ϑ by choosing, for the i-th particle, $r_i = a R_{r,i}$ $(0 \leqslant R_{r,i} \leqslant 1)$ and $\vartheta_i = 2\pi R_{\vartheta,i}$ $(0 \leqslant R_{\vartheta,i} \leqslant 1)$, and taking the R_r's and the R_ϑ's as they result from a radix-two and a radix-three digit reversal;[44] (d) the toroidal angle is randomly fixed within a one-cell-wide toroidal slice; (e) the distribution is exactly replicated for each toroidal slice; (f) volume-element and weight factors are determined in such a way as to take properly into account the inhomogeneities of the initial phase-space discretization (the initial phase-space density of simulation ''particles'') and to make the initial physical distribution function coincident with $\overline{F}_{H0}$. Steps (c) and (d) aim to preserve the local Maxwellian character of the velocity-space distribution function; steps (b) and (e) to enforce the even $\overline{U}$-parity and the axisymmetry of the equilibrium distribution function, respectively, in order to avoid spurious beam instabilities and nonaxisymmetric perturbations to the plasma equilibrium.

The field solver for the $O(\epsilon^3)$ reduced MHD equations[29,27] is based on a previous $O(\epsilon^2)$ version.[45] The code uses finite difference in the minor radius direction and Fourier expansion in the poloidal and toroidal directions. The equilibrium is calculated, to the desired order in ϵ, from the Grad–Shafranov equation, by assigning a q-profile, which determines the symmetric $(m=0, n=0)$ zeroth-order Fourier component of the magnetic-flux function ψ, and integrating the equation for the first-order correction $(m=1, n=0)$. The coupled equations for the Fourier components of the magnetic stream function ψ and the scalar potential ϕ are integrated using a semi-implicit algorithm where all the linear terms that couple with the $m=0, n=0$ equilibrium component are treated implicitly.

Field values at each particle position are obtained by trilinear interpolation of the fields at the vertices of the cell to which the particle belongs. The corresponding trilinear weight function is adopted, after pushing the particles, in order to distribute their contribution to the pressure tensor components among the vertices of the cell.

Particle pushing is performed by integrating Eqs. (3) and (17) by a second-order Runge–Kutta method. Defining $\zeta_i \equiv (\overline{Z}_i, \overline{w}_i, \overline{\Delta}_i)$ the complete set of simulation coordinates of the i-th particle and $\zeta \equiv (\zeta_1, \zeta_2, \ldots, \zeta_{N_{part}})$ the whole set of coordinates of the entire simulation population, we can synthetically indicate the pushing equations as

$$\frac{d\zeta_i}{dt} = g[\zeta_i, \Pi(\zeta)], \tag{21}$$

where the ''velocity'' g shows an explicit dependence on the particle coordinates ζ_i and an implicit dependence on the whole set ζ through the fields (here indicated by Π to keep a memory of the pressure tensor term which couples particles and fields).

Time integration of Eq. (21) yields

$$\zeta_i(t+\Delta t) = \zeta_i(t) + \Delta t\, g[\zeta_i(t), \Pi(\zeta(t))] + \frac{1}{2}(\Delta t)^2 \left. \frac{dg}{dt} \right|_t + O(\Delta t^3), \tag{22}$$

with

$$\frac{dg}{dt} = \left. \frac{\partial g}{\partial \zeta_i} g[\zeta_i, \Pi(\zeta)] \right|_t + \left. \frac{\delta g}{\delta \Pi} \sum_{l=1}^{N_{part}} \frac{\partial \Pi}{\partial \zeta_l} g[\zeta_l, \Pi(\zeta)] \right|_t. \tag{23}$$

Noting that

$$g[\zeta_i(t),\Pi(\zeta(t-\Delta t))] = g[\zeta_i,\Pi(\zeta)]|_t - \Delta t \frac{\delta g}{\delta \Pi} \sum_{l=1}^{N_{part}} \frac{\partial \Pi}{\partial \zeta_l} g[\zeta_l,\Pi(\zeta)] \Bigg|_t + O(\Delta t^2), \tag{24}$$

we can cast Eq. (22) in the following form:

$$\zeta_i(t+\Delta t) = \zeta_i(t) + \frac{3}{2}\Delta t g[\zeta_i,\Pi(\zeta)]|_t - \frac{1}{2}\Delta t g[\zeta_i(t),\Pi(\zeta(t-\Delta t))] + \frac{1}{2}(\Delta t)^2 \frac{\partial g}{\partial \zeta_i} g[\zeta_i,\Pi(\zeta)]\Big|_t + O(\Delta t^3). \tag{25}$$

Finally, defining

$$\begin{aligned} k_1 &\equiv \Delta t g[\zeta_i(t),\Pi(\zeta(t))], \\ k_2 &\equiv \Delta t g[\zeta_i(t)+k_1,\Pi(\zeta(t))], \\ k_0 &\equiv \Delta t g[\zeta_i(t),\Pi(\zeta(t-\Delta t))], \end{aligned} \tag{26}$$

and observing that

$$k_2 = k_1 + (\Delta t)^2 \frac{\partial g}{\partial \zeta_i} g[\zeta_i,\Pi(\zeta)]|_t + O(\Delta t^3), \tag{27}$$

we obtain

$$\zeta_i(t+\Delta t) = \zeta_i(t) + k_1 + \frac{1}{2}(k_2 - k_0) + O(\Delta t^3). \tag{28}$$

Note that compared with the standard pushing technique, based on the Euler method [which corresponds to retain only the first two terms in the RHS of Eq. (28)], such a Runge–Kutta scheme is more accurate [$O(\Delta t^2)$ is properly retained], although computationally more expensive. Calculations of k_2 and k_0 requires us indeed to compute the ''velocities'' also in correspondence of the shifted coordinates, $\zeta_i(t)+k_1$, or the previous-step fields, $\Pi(\zeta(t-\Delta t))$, respectively.

Quasi-cylindrical coordinates (r,ϑ,φ) are adopted in particle pushing and pressure computation, except for a limited region close to $r=0$, where rectangular coordinates (R,Z) are used to describe the meridian plane, in order to avoid singularities.

Particles that hit the wall $(r=a)$ are considered lost and are not re-injected in the plasma.

The code allows us to switch from δF to a full-F algorithm, in order to fully exploit the respective advantages of the two methods. The δF algorithm is indeed suited for linear or small-perturbation nonlinear simulations, but it can present serious problems in situations in which a high-level turbulence produces a large net displacement of physical particles. These situations indeed correspond, on one side, to a large perturbation of the distribution function,

$$\overline{\delta F_H} \to -\overline{F}_{H0}, \tag{29}$$

and, on the other side, to a rarefaction of simulation ''particles'' in the considered region. Although, in principle, there should be no difficulty in describing large-perturbation conditions (the δF algorithm does not rely on any approximation), the simulation-particle rarefaction makes the discretized representation of $\overline{\delta F_H}$ [see Eq. (10)] very poor and unable to accurately reproduce the cancellation condition, Eq. (29). Such cases are better described by full-F simulations: the lack of simulation ''particles'' in a certain region automatically corresponds to $\overline{F}_H \approx 0$, in spite of a poor discrete representation. Switching from δF to full-F simulation can then be accomplished, at a given time step, by setting

$$\overline{w}_l|_F = \overline{w}_l|_{\delta F} + \overline{\Delta}_l|_{\delta F} \overline{F}_{H0}(t,\overline{Z}_l), \tag{30}$$

and converting to the appropriate evolution equation for the weight factor [the upper side of Eq. (17)].

B. Perturbative treatment

In order to compare the self-consistent-simulation results to those obtained in the framework of models that treat the energetic-particle dynamics in a perturbative way, we also use a simplified version of the code, which will be indicated, in the following, as ''perturbative.'' Rather than solving the reduced MHD equations—Eq. (2)—for the spatial and time dependence of the fields, the fluctuating potentials are obtained, in this version, from the equations

$$\begin{Bmatrix} \phi(\overline{\mathbf{R}},t) \\ a_\parallel(\overline{\mathbf{R}},t) \end{Bmatrix} = A(t) e^{(i\omega_r - \gamma_D)t} \begin{Bmatrix} \phi_0(\overline{\mathbf{R}}) \\ a_{\parallel 0}(\overline{\mathbf{R}}) \end{Bmatrix}, \tag{31}$$

with

$$\frac{dA}{dt} = \gamma_H A(t), \tag{32}$$

where $\phi_0(\overline{\mathbf{R}})$ and $a_{\parallel 0}(\overline{\mathbf{R}})$ are given mode structures for the scalar and parallel vector potential, respectively, ω_r and γ_D are the fixed real frequency and damping rate, respectively, and γ_H represents the energetic-particle contribution to the mode growth rate. Following Ref. 4, γ_H is obtained, from a variational principle, in terms of the energetic-particle contribution to the potential energy δW_K and of the plasma kinetic energy K_M, as

$$\gamma_H \simeq \Im \lim_{\Im\omega \to 0} \delta W_K / K_M \simeq \frac{1}{2R_0} \frac{B_0}{c m_i n_0} \Re \frac{\int d^3 r \hat{\mathbf{b}} \times (\nabla \cdot \mathbf{\Pi}_H) \cdot \nabla \phi^*}{\int d^3 r |\nabla_\perp \phi|^2}. \tag{33}$$

Note that separating spatial and time dependencies, as in Eq. (31), corresponds to neglecting the feed-back of the energetic particles on the mode structure. Particle orbits are instead fully retained, as in the complete version of the code.

This treatment closely resembles that of Refs. 46–48, with a negligible difference: the real frequency shift due to particle dynamics, neglected here, is computed there—besides the growth rate—on the basis of a perturbative expression analogous to Eq. (33).

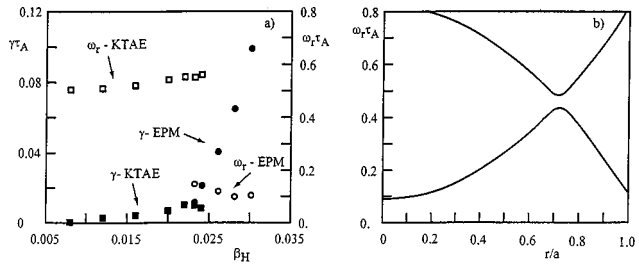

FIG. 1. Growth rate and real frequency of the most unstable modes versus β_H for linear simulations of the $n=1$ and $m=1,2$ components (a), and the corresponding shear-Alfvén continuous-spectrum (b). Here $\rho_{LH}/a=0.01$, $\alpha_n=2$, $a^2/L_n^2=2$. At low values of β_H, the KTAE (boxes) is the most unstable mode and the growth rate is weakly dependent on β_H. For $\beta_H \gtrsim 0.024$ the energetic-particle mode (circles) appears, with the growth rate sharply increasing with β_H.

IV. LINEAR RESULTS

In this section we will take the linear limit of the reduced-MHD–Vlasov system. This corresponds, in particular, to retaining only the unperturbed characteristics in the left hand side of Eq. (8) and neglecting the nonlinear contributions in the source term, Eq. (19).

For the sake of simplicity, only the circulating-particle dynamics is included: the mirroring term, proportional to $\hat{\mathbf{b}}\cdot\nabla \ln B$, is neglected in the evolution equation for the parallel velocity $\overline{U}$, Eq. (3).

Simulations refer to an equilibrium magnetic field characterized by $\psi_{eq}(r,\vartheta)=\psi_{eq_{0,0}}(r)+\psi_{eq_{1,0}}(r)\cos(\vartheta)$—corresponding to shifted circular magnetic surfaces—with inverse aspect ratio $a/R_0=0.1$ and the q-profile approximately given, in the cylindrical approximation, by $q(r)\simeq q(0)+[q(a)-q(0)]r^2/a^2$, with $q(0)=1.1$ and $q(a)=1.9$. Perturbations to $\psi_{0,0}$ and $\psi_{1,0}$ are neglected in the frame of linear simulations.

In Ref. 19 the results of linear simulations with a fixed value of β_H—the energetic-particle pressure parameter—and toroidal number $n=1$ were reported. It was shown that, in correspondence to the explored parameter regime, the TAE is stable, or very close to marginal stability, while the upper branch of the KTAE is unstable. In Fig. 1(a) the growth rates of the most unstable modes are now plotted, along with the corresponding real frequencies, at different values of β_H. The other parameters are the following: $\rho_{LH}/a=0.01$, $\alpha_n=2$, $a^2/L_n^2=2$, $\eta R_0/(a^2 v_A)=10^{-5}$. A spatial grid of $N_r\times N_\vartheta\times N_\varphi=32\times 16\times 8$ cells has been used, with an average number of 64 particles per cell. Perturbations with two coupled components—$m=1,2$—are taken into account for ψ and ϕ. With the equilibrium considered here, these two components are indeed the only ones that yield a gap structure in the shear-Alfvén spectrum. The gap is localized at $r\simeq 0.7a$, as shown in Fig. 1(b).

From Fig. 1 it is evident that two different regimes can be identified. At low values of β_H, the KTAE is the most unstable mode. The real frequency ω_r of the mode comes out to be close to the upper boundary of the gap and the mode structure—shown in Fig. 2 for $\beta_H=0.02$—exhibits its sharpest variation in correspondence to the gap region. This is the

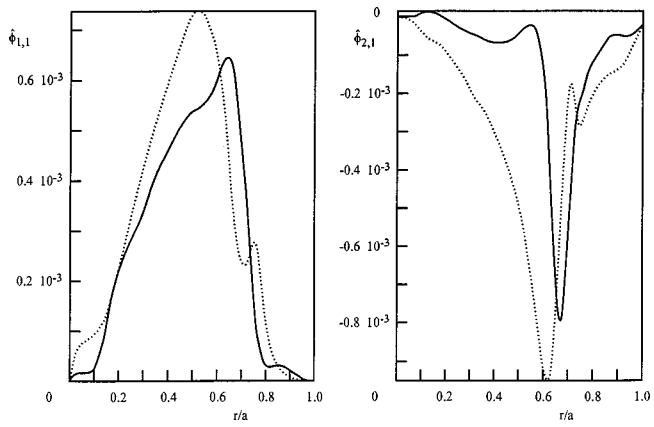

FIG. 2. Radial profiles of the real (solid line) and the imaginary (dashed line) part of the poloidal components of the perturbed scalar potential $\hat{\phi}$ ($\hat{\phi}\equiv e_H\phi/T_H$) for a simulation with $\beta_H=0.02$ and the other parameters as in Fig. 1. The two components are opposite in phase, corresponding to a KTAE-upper-branch structure, and exhibit their sharpest variation in correspondence to the gap region.

regime considered in Ref. 19. The growth rate is weakly dependent on β_H, and such that $\gamma \ll \omega_r$. Above a certain threshold in β_H ($\beta_H \approx 0.024$ in this case) a new mode appears with completely different features. Its growth rate sharply increases with β_H. The real frequency becomes very small ($\gamma \approx \omega_r$) and falls inside the lower continuum. The mode structure, shown in Fig. 3 for $\beta_H=0.03$, shows the $m=1$ and $m=2$ components localized at $r\approx 0.3a$ and $r\approx 0.8a$, respectively. Such localization appears to be quite independent of the gap position, and is determined both by the intersection of the shear Alfvén continuous spectrum with the mode frequency and the boundary conditions. The two components show even symmetry, differently from the odd-symmetry KTAE case, and consistently with the opposite localization of the real frequency with respect to the center of the gap.[19] This mode can be identified as the Energetic-Particle (beam) Mode (EPM).[20] It is evident that

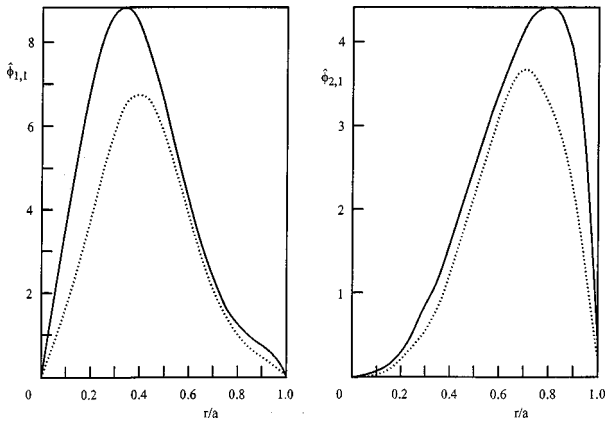

FIG. 3. Radial profiles of the scalar-potential components for a simulation with $\beta_H=0.03$. The two components are peaked quite far from the gap position. Their localization is determined instead by the boundary conditions and the intersection of the shear Alfvén spectrum with the mode frequency. The two components show even symmetry, consistently with the localization of the real frequency with respect to the center of the gap. This mode can be identified as the energetic-particle mode.

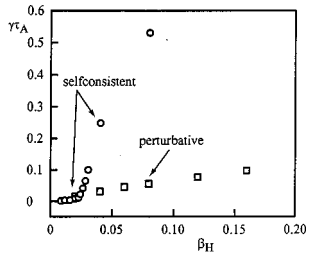

FIG. 4. The growth rate versus β_H for self-consistent (circles) and perturbative (boxes) linear simulations in the $n=1$ case. A fixed real frequency $\omega_r=0.33\ \tau_A^{-1}$ has been assumed for perturbative simulations. Perturbative results agree quite well with the self-consistent ones in the KTAE regime, but do not exhibit the EPM destabilization.

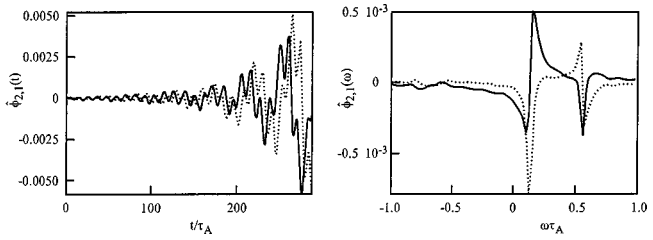

FIG. 6. Time evolution (a) and corresponding frequency spectrum (b) of the $m=2$ fluctuating scalar potential at $r=0.5\,a$, for a simulation with β_H value in the transition regime ($\beta_H=0.024$). The coexistence of unstable EPM and KTAE, with real frequencies $\omega_r\approx 0.14\ \tau_A^{-1}$ and $\omega_r\approx 0.56\ \tau_A^{-1}$, respectively, can be observed.

KTAE (or TAE) and EPM are drastically different in nature. While the KTAE (or the TAE) exists as a kinetic (or MHD) global mode and is affected by energetic particles in a perturbative way [both the mode structure and real frequency are essentially determined by the MHD terms in Eqs. (2)], the EPM exists only because of the energetic particle dynamics. Its growth, localization and real frequency are, in fact, determined by the competition between energetic-particle resonant drive and continuum damping. In this respect, they are not related to the presence of a frequency gap that, on the contrary, is needed for the formation of MHD/kinetic global modes.

These features of the EPM strongly limit the validity of any perturbative approach to the problem of the stability of shear-Alfvén modes. The results of ''perturbative'' simulations, described in Sec. III B, are compared with those of the self-consistent simulations in Fig. 4. The potential profiles $\phi_0(\overline{\mathbf{R}})$ and $a_{\|0}(\overline{\mathbf{R}})$, adopted in such perturbative simulations, correspond to $n=1$ KTAE-like eigenmodes, and are shown in Fig. 5. A fixed value $\omega_r=0.33\ \tau_A^{-1}$ (where $\tau_A\equiv R_0/v_A$) has been assumed for the real frequency. It is evident that, while the two treatments agree quite well in the KTAE regime, the EPM destabilization cannot be reproduced in the perturbative framework.

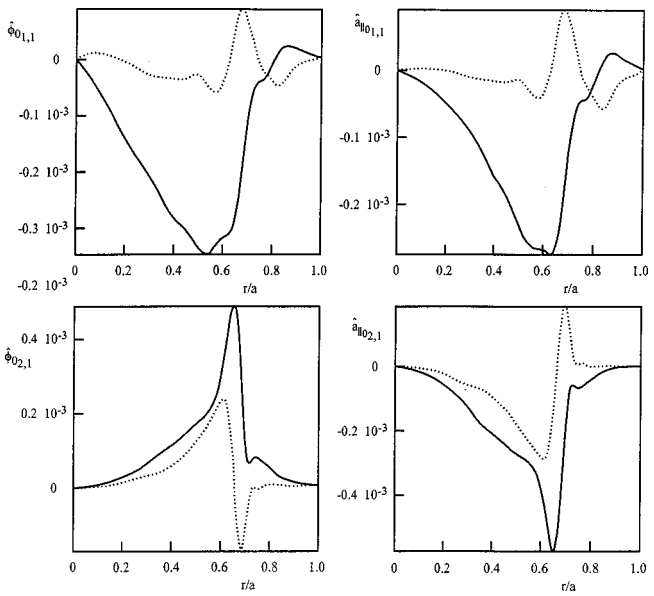

FIG. 5. Radial profiles of the scalar and parallel vector potential adopted in the perturbative simulations, corresponding to an $n=1$ KTAE-like configuration.

The results on the transition from gap modes (TAE's and KTAE's) to continuum modes (EPM's) seem consistent with those obtained by Santoro and Chen in the high-n limit.[30] Note that, on the basis of the present investigation, such a transition cannot be described as a smooth one. The coexistence of the two modes, with sharply different real frequencies, can indeed be observed in the transition regime, where the respective growth rates are of the same order. Figure 6 shows the time evolution (a) of the $m=2$ component of the fluctuating scalar potential and the corresponding frequency spectrum (b) at $r=0.5\,a$, for $\beta_H=0.024$. Both EPM and KTAE are visible, with real frequencies $\omega_r\approx 0.14\ \tau_A^{-1}$ and $\omega_r\approx 0.56\ \tau_A^{-1}$, respectively.

Similar results are found in the case of higher—although still moderate—toroidal mode number n. In Fig. 7(a) the real frequency and the growth rate of the most unstable mode at different β_H values are reported as obtained from simulations of the linear evolution of modes with $n=4$. Poloidal components with m ranging from 4 to 8 have been retained, as they give rise, for the considered q profile, to frequency gaps in the shear-Alfvén continuous spectrum properly contained inside the plasma volume. Such continuous spectrum is shown in Fig. 7(b).

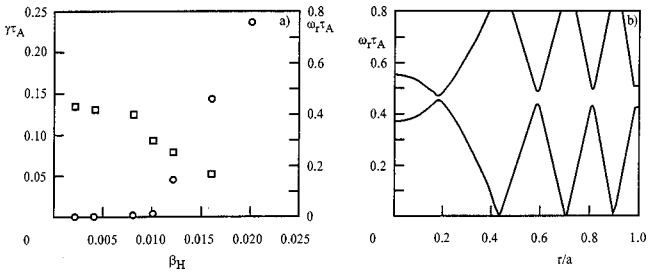

FIG. 7. Real frequency (boxes) and growth rate (circles) of the most unstable mode at different β_H values for linear simulations of modes with $n=4$ and m ranging from 4 to 8 (a), and the corresponding shear-Alfvén continuous-spectrum (b). The real frequency for $\beta_H=0.02$ is too low, compared with the growth rate, to be appreciated from the numerical-simulation results. Note that the threshold for the EPM destabilization is much lower than the $n=1$ case.

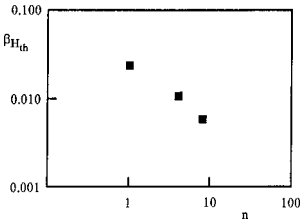

FIG. 8. Threshold β_H value for the destabilization of the EPM at different values of the toroidal mode number n. The results corresponding to $n=8$ should be considered just as indicative ones, because of the reduced velocity-space resolution achieved in the corresponding high-spatial-resolution simulations.

By comparison with the $n=1$ results, it can be noted that the destabilization of an EPM with real frequency deeply inside the lower continuum and a sharply increasing growth rate is observed, in this case, at much lower values of β_H (in fact, for $\beta_H=0.02$, the real frequency is so low, compared with the growth rate, that it cannot be determined on the basis of the numerical-simulation results).

The dependence of the threshold β_H value for the EPM destabilization on the toroidal mode number can also be appreciated from Fig. 8, where the results obtained from simulations relative to the $n=8$ case are also reported. It approximately corresponds to $\beta_{H_{th}} \propto n^{-2/3}$.

We can analyze these findings in the light of what can be argued on the basis of approximate theoretical considerations. For the sake of simplicity, we assume that the continuum damping of the mode does not depend on n; this is a good approximation only for the highly localized high-n modes, but it should not significantly affect our qualitative conclusions even if applied to the general case. As to the energetic-particle drive, close to the threshold it comes out to be proportional to β_H.[20] Furthermore, it has been shown[7,20–23] that it grows linearly with n for low n values, while it decreases as n^{-3} in the large-n limit. By balancing damping and drive terms, $\beta_{H_{th}}$ can be predicted to decrease as n^{-1} for low-n modes and to increase as n^3 at large n. The threshold β_H value is then expected to reach a minimum at some intermediate value of n. Our numerical results show that such a minimum is not yet reached up to $n=8$, so that higher-n modes can be expected to have an even lower excitation threshold.

It should also be observed, however, that, due to the limited computational resources, the high spatial resolution required by these simulations has been achieved at the expenses of the velocity–space resolution. The determination of the threshold then suffers, in this case, a higher numerical noise, and it should be considered just as indicative.

V. NONLINEAR SATURATION

Besides offering insight in the linear properties of shear-Alfvén modes, the hybrid MHD-gyrokinetic simulation allows us to investigate the problem of their nonlinear saturation and, in particular, the related effects on the confinement of energetic particles. Several mechanisms have been proposed in the literature as possible candidates for explaining the saturation of such modes. Hahm and Chen,[25] for example, have shown that the nonlinear interaction between two TAE's can produce a ponderomotive $\delta\mathbf{J}_\perp \times \delta\mathbf{B}_\perp$ force, which drives low-phase-velocity density fluctuations. Such ''virtual'' sound-wave-like fluctuations can transfer energy to bulk ions through resonant wave–particle interactions eventually leading to TAE saturation. Zonca *et al.*[26,27] have in turn shown that saturation can occur due to nonlinear modification of the equilibrium magnetic field and hence of both gap and mode structures.

A different approach to the saturation problem consists in investigating particle nonlinear dynamics. In fact, the scope of the present paper is to analyze these aspects. Thus, we start neglecting all MHD nonlinearities, although the Hybrid MHD-Gyrokinetic Code allows us to simultaneously study both mode–mode couplings and particle nonlinear dynamics on the same footing.

Wu and coworkers[46,47] and Borba *et al.*[48] have investigated particle nonlinearities through numerical simulations based on a Hamiltonian guiding-center representation of the particle motion. To the same purpose, Park *et al.*[31] have developed a hybrid MHD-gyrokinetic code, conceptually similar to the code discussed in the present paper. Meanwhile, Todo *et al.*[49] have adopted a hybrid MHD-Vlasov approach, computing the energetic-particle distribution function in an Eulerian frame, unlike the usual particle codes, which are Lagrangian in nature.

All of these authors (cf. also Ref. 50) found reasonable agreement between the simulation results and the theoretical ones, obtained by Berk and Breizmann[24] by assuming that saturation is due to nonlinear trapping of the resonant energetic particles in the potential well of the wave.

The Berk and Breizmann model can be summarized as follows. Let us define the wave phase $\Psi_{m,n}$ for a particle at the position (r,ϑ,φ) at the time t:

$$\Psi_{m,n} \equiv \omega_r t - m\vartheta + n\varphi. \tag{34}$$

In the linear case (unperturbed particle orbits), the resonant energy exchange between the wave and the particle takes place in a radial shell centered around the resonant surface and qualitatively defined by the condition

$$\left|\frac{d\Psi_{m,n}}{dt}\right| \lesssim \gamma_L, \tag{35}$$

with γ_L being the linear growth rate of the wave.

When the nonlinear effects of the wave on the particle motion are included, two different kind of trajectories exist: closed orbits for particles trapped in the potential well of the wave and open ones for untrapped particles. Trapped particles are effectively subtracted to the drive, because their energy exchange with the wave is averaged to zero in the back-and-forth motion along the $\Psi_{m,n}$ axis. The separatrix between the two families of orbits has maximum radial width proportional to the square root of the wave amplitude. The growth rate of the wave is then progressively weakened as the amplitude increases. Saturation is eventually reached when the separatrix width becomes of the same order of the width of the resonant shell defined by Eq. (35). This condition can be translated in a relationship between the saturation

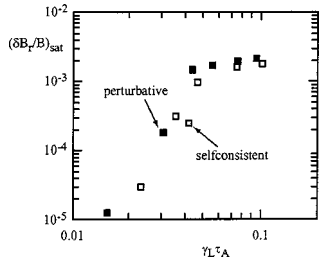

FIG. 9. The maximum amplitude of the fluctuating radial magnetic field versus linear growth rate for perturbative (full boxes) and self-consistent (empty boxes) $n=1$ simulations, performed at different values of β_H. The other parameters are the same ones considered in the rest of the paper. The departure, at moderately high γ_L values, from the very-low-γ_L scaling of the saturated amplitude can be traced back to the finite mode radial width compared to that of the resonance region.

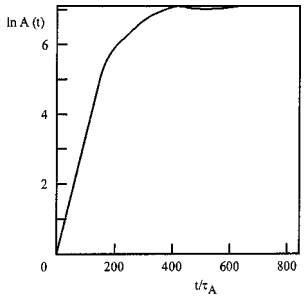

FIG. 10. Time evolution of the amplitude of the mode for a perturbative nonlinear simulation with $\gamma_D=0.01\ \tau_A^{-1}$, $\beta_H=0.08$ and the other parameters as in Fig. 4.

amplitude of the fluctuating radial magnetic field and the linear growth rate. Berk and Breizmann found,[24] under quite general hypotheses,

$$\frac{\delta B_r}{B_0} \propto \gamma_L^2 . \tag{36}$$

It is worth noting that, in the above model, particle contribution is treated perturbatively, in the sense that it only affects the growth rate, without determining neither the real frequency nor the mode structure, which can be thought as given by the dynamics of the core plasma. Consistently with this approach, Refs. 46–48 neglect the effects of the energetic-particle dynamics on the mode structure and on the zeroth-order real frequency and, in fact, obtain results in agreement with Eq. (36). From the discussion of the previous section, we expect that this perturbative approach is indeed adequate for investigating the saturation of the low-γ_L gap modes (TAE's) or their kinetic counterpart (KTAE's). This is confirmed by the results of Refs. 49–51, which are obtained in the framework of self-consistent (nonperturbative) simulations applied to a gap-mode regime and do not significantly depart from the findings of the Berk and Breizmann model. At the same time it is worth pointing out that the (high-γ_L) EPM dynamics, in which particle contribution is intrinsically nonperturbative, are likely characterized by a completely different phenomenology and require a more complete approach. In the following subsections this issue is further discussed by comparing the findings of nonlinear simulations performed with the perturbative version of the hybrid MHD-gyrokinetic code with those obtained with the self-consistent one.

A. Gap-mode saturation

In Sec. III B we have introduced a simplified, ''perturbative'' version of the simulation code, which allows us to retain only the effects of the energetic particles on the growth rate of the mode, neglecting those on the mode structure and on the real frequency.

Figure 9 shows the maximum amplitude of the fluctuating radial magnetic field, obtained at different values of β_H and plotted versus the corresponding values of the linear-phase growth rate γ_L. Full boxes refer to perturbative simulations, empty boxes to self-consistent ones. Only simulations in the low-γ_L regime are considered. The fair agreement between the two sets of results confirms the validity of the perturbative approach for this regime.

Two different sub-regimes can be distinguished with respect to the saturation mechanism. At very low values of γ_L, saturation can be traced back to the trapping of resonant particles, discussed above, whereas effects related to the finite mode radial width begin to play a role at slightly higher values of γ_L, as discussed later. The first sub-regime can be easily recognized by examining the findings of a typical perturbative simulation in such a sub-regime. Figure 10 shows the time behavior of the amplitude of the mode for $\beta_H=0.08$, $\gamma_D=0.01\ \tau_A^{-1}$ and the other parameters as in the simulations considered in Fig. 4. After the initial linear-growth phase, the nonlinear growth rate progressively decreases and saturation is eventually reached. The time evolutions of the radial coordinate r and the parallel velocity $\bar{U}$ are reported in Fig. 11(a) and 11(b), respectively, for an energetic particle initially satisfying the nearly-resonance condition, Eq. (35), with the $m=2$ component. During the whole linear phase ($t<150\ \tau_A$) the particle orbit is almost unperturbed. The oscillation of the particle radial position is due to the effect of the toroidal equilibrium. The significant decrease of γ_H coincides with a strong modification of the original linear evolution. Figure 12 shows the trajectories in the plane $(\Psi_{2,1},r)$, for the same particle, in the time intervals $0<t<284\ \tau_A$ (a) and $264\ \tau_A<t<560\ \tau_A$ (b) (note that

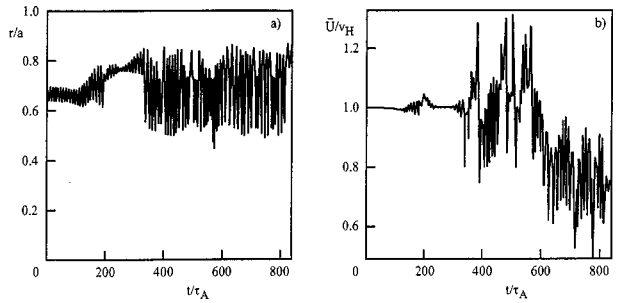

FIG. 11. Time evolution of the radial coordinate (a) and the parallel velocity (b) of a nearly-resonant (with respect to the component $m=2$) energetic particle, for the case of Fig. 10. During the linear-growth phase the orbit remains almost unperturbed. The saturation phase coincides with a significant alteration of the original evolution.

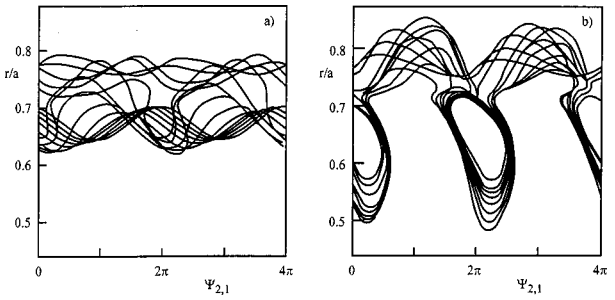

FIG. 12. The orbit in the plane $(\Psi_{2,1},r)$, for the same particle as in Fig. 11, in the time intervals $0<t<284\tau_A$ (a) (linear growth) and $264\ \tau_A<t<560\ \tau_A$ (b) (nonlinear saturation). The $\Psi_{2,1}$ axis is mapped onto the interval $0\leqslant\Psi_{2,1}<4\pi$. The particle is initially passing, but becomes trapped as the mode reaches a certain amplitude.

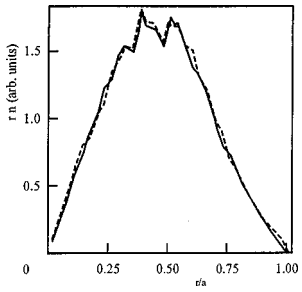

FIG. 14. Energetic-particle line-density profile, in the same simulation as in Fig. 13, at $t=30\tau_A$ (solid line), during the linear growth of the mode, and at $t=480\tau_A$ (dashed line), after that saturation has been reached. No appreciable modification can be observed.

the two intervals are slightly overlapping). For the sake of clarity, the $\Psi_{2,1}$ axis is mapped onto the interval $0<\Psi_{2,1}<4\pi$. It is evident that, during the linear phase, the trajectory corresponds to that of a passing particle, while, when the mode amplitude reaches a certain level, the particle becomes trapped, stops contributing to the drive and takes indirectly part to the mode saturation.

Similar conclusions can be drawn, as expected, from the results of the self-consistent simulations. In Fig. 13, the time evolution of the poloidal spectrum of the total fluctuating energy for $\beta_H=0.02$ is plotted. Figure 14 shows, for the same case, the normalized energetic-particle line-density profile $[\propto rn_H(r)]$ at two different times in the simulation: the solid line refers to $t=30\tau_A$, during the linear growth of the mode; the dashed line to $t=480\tau_A$, after that saturation has been reached. There is no appreciable modification in the density profile, consistently with the conjecture of a ''soft'' trapping mechanism.

For higher (although still moderate) values of γ_L, a second ''perturbative'' saturation sub-regime can be identified. In fact, the γ_L dependence of $\delta B_r|_{sat}$ tends to become weaker, due to the fact that the radial width of the resonance region (proportional to γ_L) tends to exceed the (finite) mode radial width. The fraction of resonating particles is then cut off, and saturation is reached at almost constant values of $\delta B_r|_{sat}$, irrespectively to the value of γ_L.

Finally, it should be also observed that the scaling $\delta B_r|_{sat}\propto\gamma_L^{\alpha}$, with $\alpha\lesssim 4$, obtained in the very-low-γ_L sub-regime differs from that[24] reported in Eq. (36) and obtained also in Refs. 46–49. Although a thorough interpretation of this discrepancy is still lacking, it is possible to conjecture that the finite growth rates considered here do not allow us to make straightforward comparisons with the vanishing-γ_L approach of Ref. 24. Note that also the results of Ref. 51 depart from the γ_L^2 scaling as higher values of the growth rate $(\gamma_L/\omega\gtrsim 2\%)$ are considered, although those authors suggest to interpret such a discrepancy in terms of overlapping of multiple TAE's.

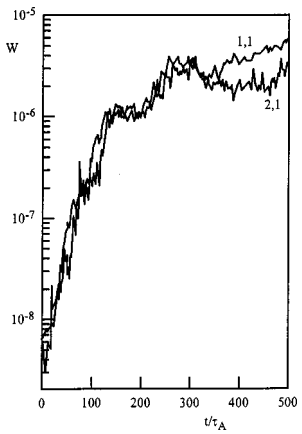

FIG. 13. The time evolution of the poloidal components of the total fluctuating energy for an $n=1$, $\beta_H=0.02$ self-consistent nonlinear simulation.

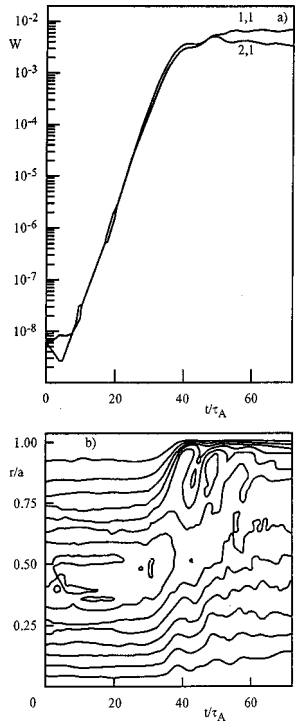

FIG. 15. The time evolution of the poloidal components of the total energy (a), and the contour plot of the line-density in the (t,r) plane (b) for a self-consistent simulation with $\beta_H=0.04$ (EPM regime). Saturation occurs because of an abrupt displacement of the energetic-particle population.

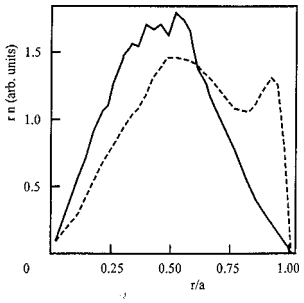

FIG. 16. The line-density profile at $t=20\tau_A$ (solid line), during the linear growth of the mode, and at $t=40\tau_A$ (dashed line), after saturation, for the simulation shown in Fig. 15. A macroscopic displacement of the source of instability is observed.

B. EPM saturation

The investigation of the EPM saturation cannot, in general, be performed within a perturbative approach and requires fully self-consistent simulations. The time evolution of the total energy for such a simulation for $\beta_H=0.04$ is reported in Fig. 15(a), along with the contour plot of the line-density in the (t,r) plane Fig. 15(b). It can be noticed that, differently from the case examined in Fig. 13, saturation occurs in coincidence with sudden displacement of the source of instability (the energetic-particle population). This macroscopic displacement can be observed also from Fig. 16, showing the line-density profile before (solid line) and after (dashed line) saturation, and can be traced back to the secular radial drift that affects the energetic-particle motion, shown in Fig. 17 for a particle with initial radial coordinate $r=0.4\,a$.

The secular radial drift induced on the circulating particles in resonance with the wave is of the same type discussed in Ref. 52 for the *fishbone* mode, although we are reminded that fishbone oscillations are typically driven unstable by resonant interactions with the magnetically-trapped energetic particles. Nevertheless, the analogy is worth being drawn since Fig. 15 is clear evidence of the fact that the secular radial motion becomes a larger at larger mode amplitude, in agreement with the mechanism called ''mode-particle pumping'' and discussed in Ref. 53. Furthermore, Fig. 15 also indicates that the secular radial motion becomes negligible for particles located at radial positions where the mode amplitude is also negligible.[53] This fact explains the

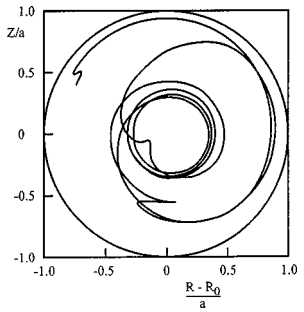

FIG. 17. Poloidal-plane projection of a typical energetic-particle orbit, with initial radial coordinate $r=0.4\,a$, in the simulation of Fig. 15.

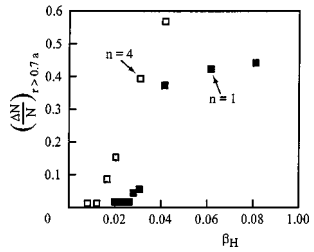

FIG. 18. Fraction of the global energetic-particle population displaced out of $r=0.7a$ in self-consistent simulations with toroidal number $n=1$ (full boxes) and $n=4$ (empty boxes).

formation of a sharp energetic-particle density gradient at the plasma boundary. It also emphasizes that a consistent description of appreciable particle losses through the plasma boundary would require the inclusion of ''external'' poloidal harmonics (with $m/n=1>q$) coupled to the fundamental $m=1,2$ EPM components. This is, however, beyond the purpose of the present analysis, which is mainly to point out that significant energetic-particle redistributions are associated to the EPM destabilization, and that these are responsible for the mode saturation in the present picture.

Incidentally, we note that nonlinear saturation in our model for the EPM is steady state since we chose not to include a finite background dissipation and a source term in the Vlasov equation for the energetic particles. Would have we done so, we could recover ''bursting'' cycles of the EPM instability and of the associated particle losses.[52,54]

The issue of particle redistributions associated to EPM's is analyzed in Fig. 18, which shows the fraction of the global energetic-particle population displaced out of a fixed radial

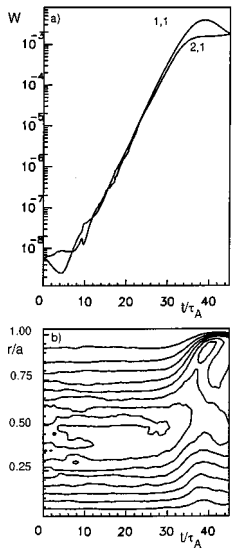

FIG. 19. Time evolution of the $n=1$ poloidal components of the total energy (a), and contour plot of the line-density in the (t,r) plane (b) for a simulation analogous to that shown in Fig. 15, but including the MHD nonlinearities. An artificial viscous term has been introduced in the fluid equations and a larger resistivity value has been fixed $[\eta R_0/(a^2 v_A)=10^{-3}]$ in order to prevent numerical instabilities due to the explicit character of the nonlinear MHD terms.

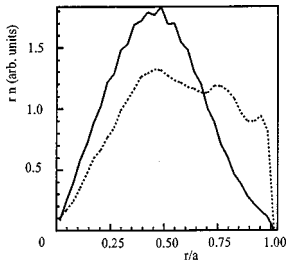

FIG. 20. The initial (solid line) and final (dashed line) line-density profile for the simulation shown in Fig. 19.

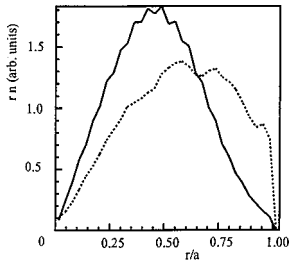

FIG. 22. The initial (solid line) and final (dashed line) line-density profile for the simulation shown in Fig. 21.

position ($r=0.7a$, in this case). Results obtained in self-consistent simulations with toroidal number $n=1$ (full boxes) and $n=4$ (empty boxes) are plotted.

The inclusion of MHD nonlinearities is not expected to appreciably modify these results. Indeed, it has been shown[26,27] that such nonlinearities mainly alter the shear-Alfvén continuum in the region close to the gap. Such a modification can influence the continuum damping of gap modes and, eventually, yield their saturation. The existence of EPM's and their dynamics are weakly affected by the presence of the gap; thus, we can guess that the EPM saturation mechanism, described here, remains effective even if the MHD nonlinear terms are fully taken into account in the simulation. This seems to be confirmed by the results shown in Figs. 19 to 22, where two simulations are compared, respectively with and without MHD nonlinearities. Only the nonlinear evolution of the (1,0), (1,1), (2,1) and (3,2) harmonics has been included, which is justified as it is discussed in Refs. 26 and 27. This choice allows us to take into account the main MHD nonlinear effects and, in particular, the continuous spectrum alteration in the gap region. No significant difference can be appreciated for both the saturation level [see Figs. 19(a) and 21(a)] and the particle-displacement mechanism [see Figs. 19(b) and 21(b), and Figs. 20 and 22]. Note that an artificial viscous term has been introduced in the fluid equations and a larger resistivity value has been fixed [$\eta R_0/(a^2 v_A)=10^{-3}$] with respect to the case shown in Fig. 15 in order to prevent numerical instabilities due to the explicit character of the nonlinear MHD terms. The simulation runs over a time interval of the order of 5% of the resistive time, and the related violation of the frozen-in flux condition must be taken into account in evaluating these results, which, however, should maintain their full qualitative validity.

In summary, several facts deserve to be emphasized. First, the macroscopic displacement of energetic particles is effectively caused by the EPM destabilization, as demonstrated by the high correlation degree between the displaced fraction and the linear-phase growth rate shown in Fig. 23. This confirms that low-growth-rate gap modes (TAE's and KTAE's) and high-growth-rate EPM's saturate because of completely different dynamic behaviors.

Second, the inadequacy of the perturbative picture in describing the EPM regime should suggest caution in concluding, on the basis of perturbative treatments, that the Alfvén modes have little influence on energetic-particle transport and confinement.

Third, a warning must be kept in mind for the results of these self-consistent simulations, because deteriorated confinement properties are observed above the β_H threshold for the EPM destabilization, which, in the $n=1$ case, is unrealistically high (with the parameters considered in this paper, $\beta_H|_{th}\approx 0.024$). However, from the $n=4$ and $n=8$ results, it is evident that such a threshold is characterized by a relevant dependence on the toroidal mode number: in fact, in these cases we find $\beta_H|_{th}\approx 0.011$ and $\beta_H|_{th}\approx 0.006$, respectively, although the latter result should be considered just as an indicative one. It has been suggested, in Refs. 55–57 that

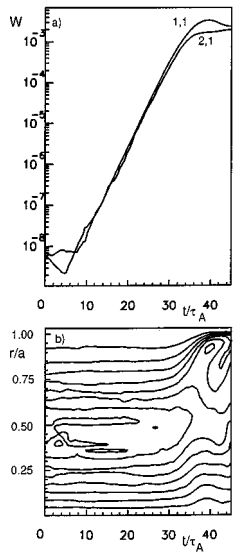

FIG. 21. The same as Fig. 19, without MHD nonlinearities. No appreciable difference is observed in the saturation mechanism in the two cases. Note that the simulation differs from that of Fig. 15 only for the inclusion of a viscous term and for a larger resistivity value.

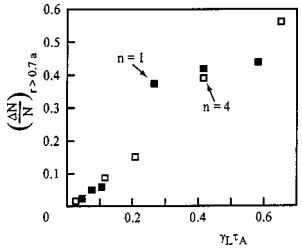

FIG. 23. The same quantities of Fig. 18 plotted versus the corresponding values of the linear-phase growth rate γ_L. A high degree of correlation is observed.

EPM's with $n \gtrsim 10$ can, in fact, be unstable in realistic plasmas close to ignition conditions. High resolution self-consistent simulations are then required to check whether the qualitative features of EPM dynamics discussed here are still relevant in such a high-n regime and, most of all, whether the β_H threshold for confinement deterioration of charged fusion products may be significantly low for realistic ignited-plasma conditions.

VI. CONCLUSIONS

In this paper we have presented the results of numerical simulation, performed with the Hybrid MHD-gyrokinetic Code, of linear and nonlinear behavior of shear-Alfvén modes in tokamaks. It has been pointed out that for β_H greater than a certain threshold value $\beta_{H_{th}}$ the EPM becomes unstable, with the growth rate fast increasing with β_H. The frequency of the mode is mainly determined by the resonance condition with the energetic particles, and falls inside the lower continuum, with poor correlation with the gap location. The EPM stability cannot then be studied as the effect of a perturbative contribution of the energetic particles to an existing MHD mode. An important result of the present investigation concerns the determination of the threshold for EPM destabilization: it has been shown that $\beta_{H_{th}}$ has a sensitive inverse dependence on the toroidal mode number n of the considered fluctuations. Although, for limitations related to computational resources, our results regard only the range of low up to moderate values of n, it can be argued that high-n EPM's could be unstable in realistic tokamak conditions, especially for plasmas close to the ignition conditions.

The problem of saturation of shear-Alfvén modes and their effects on the confinement properties of energetic particles has been explored in the frame of nonlinear simulations. We have shown that the saturation mechanism is completely different for low-growth-rate modes, such as TAE and KTAE, and for fast-growing modes, such as EPM. While the former appear to saturate because of the nonlinear trapping of resonant energetic particles in the potential well of the wave, with a very weak influence on the energetic-particle transport, the latter saturates because of a macroscopic outward displacement of the energetic-particle population, with a potentially dramatic consequence on their confinement.

An accurate investigation of both stability and saturation properties of high-n shear-Alfvén modes is then required to determine whether EPM's can affect α-particle confinement in the next-generation tokamaks.

[1] M. N. Rosenbluth and P. H. Rutherford, Phys. Rev. Lett. **34**, 1428 (1975).
[2] A. B. Mikhailowskii, Sov. Phys. **41**, 890 (1975).
[3] K. T. Tsang, D. J. Sigmar, and J. C. Whitson, Phys. Fluids **24**, 1508 (1981).
[4] R. Betti and J. P. Freidberg, Phys. Fluids B **4**, 1465 (1992).
[5] L. Chen, in *Theory of Fusion Plasmas*, Proceedings of the Joint Varenna–Lausanne International Workshop, Chexbres, Switzerland, 1988, edited by J. Vaclavik, F. Troyon, and E. Sindoni (Editrice Compositori Società Italiana di Fisica, Bologna, 1988), pp. 327–338.
[6] H. Biglari, F. Zonca, and L. Chen, Phys. Fluids B **4**, 2385 (1992).
[7] G. Y. Fu and C. Z. Cheng, Phys. Fluids B **4**, 3722 (1992).
[8] E. M. Barston, Ann. Phys. (N.Y.) **29**, 282 (1964).
[9] H. Grad, Phys. Today **22**, 34 (1969).
[10] C. E. Kieras and J. A. Tataronis, J. Plasma Phys. **28**, 395 (1982).
[11] C. Z. Cheng, L. Chen, and M. S. Chance, Ann. Phys. (N.Y.) **161**, 21 (1985).
[12] C. Z. Cheng and M. S. Chance, Phys. Fluids **29**, 3695 (1986).
[13] A. Hasegawa and L. Chen, Phys. Rev. Lett. **35**, 370 (1975).
[14] A. Hasegawa and L. Chen, Phys. Rev. Lett. **36**, 1362 (1976).
[15] R. R. Mett and S. M. Mahajan, Phys. Fluids B **4**, 2885 (1992).
[16] J. Candy and M. N. Rosenbluth, Bull. Am. Phys. Soc. **37**, 1558 (1992).
[17] H. L. Berk, R. R. Mett, and D. M. Lindberg, Phys. Fluids B **5**, 3969 (1993).
[18] F. Zonca, Plasma Phys. Controlled Fusion **35**, 307 (1993).
[19] S. Briguglio, G. Vlad, F. Zonca, and C. Kar, Phys. Plasmas **2**, 3711 (1995).
[20] L. Chen, Phys. Plasmas **1**, 1519 (1994).
[21] H. L. Berk, B. N. Breizman, and H. Ye, Phys. Lett. A **162**, 475 (1992).
[22] S. T. Tsai and L. Chen, Phys. Fluids B **5**, 3284 (1993).
[23] F. Zonca and L. Chen, Phys. Plasmas **3**, 323 (1996).
[24] H. L. Berk and B. N. Breizman, Phys. Fluids B **2**, 2246 (1990).
[25] T. S. Hahm and L. Chen, Phys. Rev. Lett. **74**, 266 (1995).
[26] F. Zonca, F. Romanelli, G. Vlad, and C. Kar, Phys. Rev. Lett. **74**, 698 (1995).
[27] G. Vlad, C. Kar, F. Zonca, and F. Romanelli, Phys. Plasmas **2**, 418 (1995).
[28] C. K. Birdsall and A. B. Langdon, *Plasma Physics via Computer Simulation* (McGraw-Hill, New York, 1985).
[29] G. Vlad, S. Briguglio, C. Kar, F. Zonca, and F. Romanelli, in Ref. 5, pp. 361–382.
[30] R. A. Santoro and L. Chen, Phys. Plasmas **3**, 2349 (1996).
[31] W. Park, S. Parker, H. Biglari, M. Chance, L. Chen, C. Z. Cheng, T. S. Hahm, W. W. Lee, R. Kulsrud, D. Monticello, L. Sugiyama, and R. White, Phys. Fluids B **4**, 2033 (1992).
[32] H. R. Strauss, Phys. Fluids **20**, 1354 (1977).
[33] R. Izzo, D. A. Monticello, W. Park, J. Manickam, H. R. Strauss, R. Grimm, and K. McGuire, Phys. Fluids **26**, 2240 (1983).
[34] W. W. Lee, Phys. Fluids **26**, 556 (1983).
[35] W. W. Lee, J. Comput. Phys. **72**, 243 (1987).
[36] T. S. Hahm, J. Fluid Mech. **31**, 2670 (1988).
[37] T. S. Hahm, W. W. Lee, and A. Brizard, Phys. Fluids B **31**, 1940 (1988).
[38] A. M. Dimits, L. L. LoDestro, and D. H. E. Dubin, Phys. Fluids B **4**, 274 (1992).
[39] T. Tajima and F. W. Perkins (private communication, 1983).
[40] T. Tajima, *Computational Plasma Physics* (Addison-Wesley, Redwood City, CA, 1989), p. 209.
[41] M. Kotschenruether, Bull. Am. Phys. Soc. **33**, 2107 (1988).
[42] S. Briguglio, G. Betello, G. Fogaccia, S. Graziadei, S. C. Guo, C. Kar, F. Romanelli, G. Vlad, and F. Zonca, in *Proceedings of the 14th International Conference on Plasma Physics and Controlled Nuclear Fusion Research 1992*, Wurzburg (International Atomic Energy Agency, Vienna, 1993), pp. 87–95.
[43] S. E. Parker and W. W. Lee, Phys. Fluids B **5**, 77 (1993).
[44] J. M. Hammersley and D. C. Handscomb, *Monte Carlo Methods* (Methuen, London, 1964), pp. 25–42.
[45] A. Bondeson, Nucl. Fusion **26**, 929 (1986).
[46] Y. Wu and R. B. White, Phys. Plasmas **1**, 2733 (1994).
[47] Y. Wu, R. B. White, Y. Chen, and M. N. Rosenbluth, Phys. Plasmas **2**, 4555 (1995).
[48] D. Borba, J. Candy, A. Fasoli, W. Kerner, D. Muir, S. Sharapov, in *Controlled Fusion and Plasma Physics*, Proceedings of the 23rd European Conference on Controlled Fusion and Plasma Physics, Kiev, Ukraine, 1996 (European Physical Society, Petit-Lancy, 1996), pp. 143–146.
[49] Y. Toda, T. Sato, K. Watanabe, T. H. Watanabe, and R. Horiuchi, Phys. Plasmas **2**, 2711 (1995).
[50] G. Y. Fu and W. Park, Phys. Rev. Lett. **74**, 1594 (1995).
[51] Y. Todo and T. Sato, in *Proceedings of the 16th International Conference on Plasma Physics and Controlled Nuclear Fusion Research 1996*, Montreal (International Atomic Energy Agency, Vienna, 1997), Vol. 2, pp. 423–430.
[52] L. Chen, R. B. White, and M. N. Rosenbluth, Phys. Rev. Lett. **52**, 1122 (1984).
[53] R. B. White, R. J. Goldston, K. McGuire, A. H. Boozer, D. A. Monticello, and W. Park, Phys. Fluids **26**, 2958 (1983).
[54] H. L. Berk, B. N. Breizman, and H. Ye, Phys. Rev. Lett. **68**, 3563 (1992).
[55] S. Briguglio, C. Kar, F. Romanelli, G. Vlad, and F. Zonca, Plasma Phys.

Controlled Fusion **37**, A279 (1995).
[56]G. Vlad, F. Zonca, and F. Romanelli, Nucl. Fusion **35**, 1651 (1995).
[57]C. Z. Cheng, H. L. Berk, D. Borba, B. Breizman, R. Budny, R. H. Bulmer, J. Candy, D. S. Darrow, A. Fasoli, E. D. Fredrikson, G. Y. Fu, R. J. Goldston, N. Gorelenkov, G. Huysmans, W. Kerner, H. Kimura, S. V. Konovalov, Y. Kusama, J. Manickam, R. Nazikian, G. H. Neilson, W. M. Nevins, T. Ozeki, L. D. Pearlstein, S. Putvinskii, M. H. Redi, F. Romanelli, M. N. Rosenbluth, S. Sharapov, D. A. Spong, K. Tobita, J. W. Van Dam, G. Vlad, R. B. White, K. L. Wong, V. Wong, F. Zonca, and S. J. Zweben, in Ref. 51, pp. 953–962.